

Chaotic wave dynamics in weakly magnetised spherical Couette flows

Ferran Garcia,^{1,2, a)} Martin Seilmayer,¹ André Giesecke,¹ and Frank Stefani¹

¹⁾*Helmholtz-Zentrum Dresden-Rossendorf, Bautzner Landstraße 400,
D-01328 Dresden, Germany.*

²⁾*Anton Pannekoek Institute for Astronomy, University of Amsterdam,
Postbus 94249, 1090 GE Amsterdam, The Netherlands.*

(Dated: 5 November 2021)

Direct numerical simulations of a liquid metal filling the gap between two concentric spheres are presented. The flow is governed by the interplay between the rotation of the inner sphere (measured by the Reynolds number Re) and a weak externally applied axial magnetic field (measured by the Hartmann number Ha). By varying the latter a rich variety of flow features, both in terms of spatial symmetry and temporal dependence, is obtained. Flows with two or three independent frequencies describing their time evolution are found as a result of Hopf bifurcations. They are stable on a sufficiently large interval of Hartmann numbers where regions of multistability of two, three and even four types of these different flows are detected. The temporal character of the solutions is analysed by means of an accurate frequency analysis and Poincaré sections. An unstable branch of flows undergoing a period doubling cascade and frequency locking of three-frequency solutions is described as well.

^{a)}f.garcia-gonzalez@hzdr.de

I. LEAD PARAGRAPH

One of the paradigms of magnetohydrodynamic flows in spherical geometry is the magnetised spherical Couette flow. An electrically conducting liquid is confined between two differentially rotating spheres and is subjected to a magnetic field. Despite its simplicity, this model gives rise to a rich variety of instabilities, and it is also important from an astrophysical point of view. The present study advances the knowledge of the dynamics of this problem by describing it in terms of dynamical systems theory, a rigorous mathematical way to understand time dependent behaviour of natural systems.

II. INTRODUCTION

The problem under consideration is the magnetised spherical Couette (MSC) flow which describes the motion of an electrically conducting liquid confined between two differentially rotating spheres and subjected to a magnetic field parallel to the axis of rotation. It is formulated in terms of the three-dimensional incompressible Navier-Stokes equations with enforced differential rotation between the rigid boundaries. This allows the appearance of thin shear layers (Stewartson layer, Ref. 1) parallel to the rotation axis, along the tangent cylinder, and thin Ekman-Hartmann boundary layers². The latter emerge in case of no-slip boundary conditions, in order to model the set up of laboratory experiments. The numerical treatment is thus extremely challenging because of the high spatial resolution required to resolve these thin layers.

The MSC system is interesting as a simple model to study how magnetic fields interact with conducting liquids in rotating spherical containers. Such interactions are important for the understanding of planetary or stellar dynamos, as referenced by Refs. 3, 4, and related experiments conducted by Ref. 5. See the review article (Ref. 6) and books (Refs. 2, 7) for detailed references and introduction to the field. The MSC system is also of interest to model the magnetorotational instability (MRI)⁸ which is believed to explain the transport of angular momentum in accretion disks around black holes and stars, and also in protoplanetary disks⁹. The transport of angular momentum in such environments seems to be the cause which allows the matter to fall into the center.

Because of its relevance, MRI has been studied experimentally, with GaInSn between two rotating cylinders at Helmholtz-Zentrum Dresden-Rossendorf (HZDR)¹⁰⁻¹², and in Maryland¹³ with liquid sodium between differentially rotating spheres. In this latter experiment the observed instabilities were considered as MRI, but with nonaxisymmetric (azimuthally dependent) symmetry. However, subsequent numerical simulations^{14,15}, and experiments¹⁶, have not interpreted the instabilities as MRI but as typical instabilities associated to the MSC system, namely the radial jet, return flow and shear layer instabilities^{17,18}. These different interpretations provide a motivation for advancing the knowledge of the MSC system.

In absence of magnetic field, and with the outer sphere at rest, the basic axisymmetric spherical Couette (SC) flow is stable¹⁹ for sufficiently small rotation of the inner sphere (measured by the Reynolds number Re). At a certain critical Re_c nonaxisymmetric instabilities give rise to regular flows whose pattern and topology depend strongly on the gap width $\chi = r_i/r_o$ (with r_i and r_o being the inner and outer radii) of the problem. When the shell is thin, Taylor-Görtler vortices develop²⁰⁻²² contrasting with the spiral waves²³⁻²⁵ preferred at wider gaps. In the latter case, triadic resonances were found in a recent study (see Ref. 26) before reaching the turbulent regime. Generally, chaotic and even turbulent flows are obtained from successive bifurcations of the initial base state if Re is sufficiently increased. This is typical in large scale dissipative dynamical systems²⁷. Although the SC system has a simple formulation, it reveals immense complexity as it has been shown in the recent study (Ref. 28) which investigates different flow regimes appearing either with positive or negative differential rotation.

In the presence of a magnetic field the axisymmetric base spherical Couette flow and its corresponding nonaxisymmetric instabilities have been determined in the (χ, Re, Ha) parameter space^{14,17}. Only a few fully nonlinear studies (e.g., Refs. 15, 29-32) have investigated the flow properties, by means of direct numerical simulations (DNS), and addressed their dependence on the physical parameters. The main differences among the latter studies rely on the topology of the applied magnetic field (axial, dipole, quadrupole) or on the type of boundary conditions considered. A comprehensive numerical study, Ref. 33, related to the liquid sodium Derviche Torneur Sodium (DTS) experiment in Grenoble³⁴, has revealed several dynamical regimes where coherent structures coexist with turbulent flows. Very recently on Ref. 35, with an inner sphere rotating slightly faster than the outer and a dipolar field due to magnetised inner sphere, axisymmetric and nonaxisymmetric solutions were

obtained. The latter have been interpreted as MRI because they are produced within the Stewartson layer and arise as a rotating wave when the helical component of the magnetic field is strong.

The HEDGEHOG (Hydromagnetic Experiment with Differentially Gyrating sphEres Holding GaInSn) laboratory experiment¹⁶ at Helmholtz-Zentrum Dresden-Rossendorf is designed to study the different flow (hydrodynamic and magnetic) instabilities occurring for a homogeneous axial applied magnetic field. This configuration has been previously addressed in the numerical studies of Refs. 14, 17, 29, 32. Beyond a critical value Re_c the basic flow becomes unstable to non-axisymmetric perturbations whose topology depends strongly on the applied magnetic field strength (measured by the Hartman number Ha). At low Ha the instability appears in the form of an equatorially antisymmetric radial jet at the equatorial plane, whereas at large Ha the instability is equatorially symmetric and connected to a shear layer at the tangent cylinder^{14,29}. For moderate values of Ha , between the radial jet and the shear layer instability, it takes the form of a meridional return flow instability¹⁴. We note that the radial jet and return flow instabilities are separated by a Ha interval in which the basic flow stabilises again^{14,17}.

From the mathematical point of view the SC and the MSC are $\mathbf{SO}(2) \times \mathbf{Z}_2$ equivariant systems, i. e., invariant by azimuthal rotations and reflections with respect to the equatorial plane. In this class of dynamical systems the type of solutions appearing at successive bifurcations from the base state is theoretically known^{36–40}.

After a primary Hopf bifurcation, several branches of periodic rotating waves (RW) appear, which in turn give rise to quasiperiodic modulated rotating waves (MRW) at a secondary Hopf bifurcations. In case of the MSC problem the existence of RW has been confirmed by experimental studies⁴¹ and by DNS^{14,15,29} but their dependence upon parameters, especially the Hartmann number, was not addressed in much detail. Only very recently, a continuation method was applied in Ref. 18 to determine extensive RW bifurcation diagrams as a function of Ha . The stability analysis of RW close to secondary bifurcation points have provided initial conditions to obtain and classify MRW⁴². The analysis of Refs. 18, 42 is performed at a moderate Reynolds number regime extending previous numerical studies^{14,17,29} by describing the type of flows in terms of bifurcation theory.

The pioneering theoretical work of Ref. 43 showed that arbitrarily smooth perturbations can destroy a three-frequency quasiperiodic solution, a solution whose temporal dependence

is described by three incommensurate frequencies, producing a strange attractor questioning the existence of such a solutions in real physical systems. Later work of Ref. 44, however, provided several numerical examples where these three frequency solutions indeed exist. The authors of Ref. 44 argue that the smooth perturbations which may destroy these three frequency solutions are unlikely to occur in practise. Subsequent studies in the context of axisymmetric Navier-Stokes flow in a cylindrical annulus⁴⁵, 2D convection in a rectangle⁴⁶, a rotating baroclinic annulus⁴⁷, or a 2D rectangular cavity filled with air⁴⁸, provided further evidence of three frequency solutions. Moreover, three frequency solutions have been found as well as in the case of 3D convection in a rotating sphere, although in a very narrow parameter range⁴⁹.

The present paper continues previous work described in Refs. 18, 42. The main novelty of the present study is to describe new branches of quasiperiodic MRW with two and even three frequencies and branches of chaotic flows. The flows with temporal dependence described by 3 frequencies are obtained for first time in the MSC problem. In addition, to the best knowledge of the authors, three frequency solutions in a three dimensional MHD problem have been never described up to now. These solutions are found when the applied axial magnetic field is weak, i. e., in the regime governed by the radial jet instability. The main goal is to describe the spatio-temporal symmetries of the waves as the Hartmann number $Ha \rightarrow 0$ is decreased. As it will be shown in the paper, several regions of multistability involving three-frequency solutions are found and their temporal scales are accurately determined by means of sophisticated time series analysis⁵⁰. This is important for later comparisons with the results of the HEDGEHOG experiment.

The organisation of the paper is as follows: Section § III introduces the model problem and the numerical method used to solve the governing equations. The core of the study belongs to § IV where the results are presented and the dynamics of the system is analysed. Finally, § V summarises the main conclusions of the study.

III. THE MAGNETISED SPHERICAL COUETTE MODEL

A liquid metal of constant density ρ , kinematic viscosity ν , electrical conductivity σ , magnetic diffusivity $\eta = 1/(\sigma\mu_0)$, μ_0 being the free-space value for the magnetic permeability, fills a spherical shell with inner and outer radii r_i and r_o . The fluid is driven by the rotation

of the inner sphere at a constant angular velocity Ω around the vertical axis $\hat{\mathbf{e}}_z$ and the outer sphere is at rest.

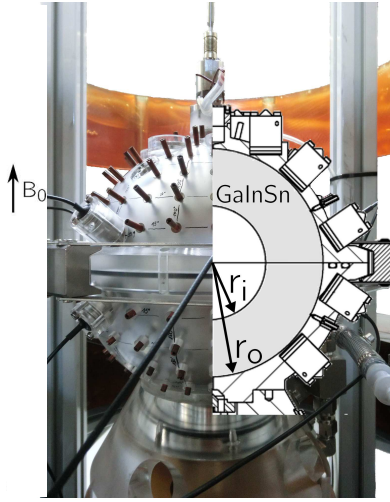


FIG. 1. Geometry of the HEDGEHOG experiment. The scheme (left side) shows the inner (rotating) and outer (at rest) spheres. On the latter, the ultrasonic Doppler velocimeter (UDV) sensors (thick cylinders) and the electric potential probes (thin needles) are attached.

In the case of the HEDGEHOG laboratory experiment, compare to Ref. 16, the flow is subjected to a uniform axial magnetic field $\mathbf{B}_0 = B_0 \hat{\mathbf{e}}_z = B_0 \cos(\theta) \hat{\mathbf{e}}_r - B_0 \sin(\theta) \hat{\mathbf{e}}_\theta$, θ being the colatitude and B_0 the magnetic field strength (Fig. 1).

Length, time, velocity and magnetic field are scaled using the characteristic quantities $d = r_o - r_i$, d^2/ν , $r_i \Omega$ and B_0 , respectively, in order to obtain the dimensionless equations. For the HEDGEHOG experiment the inductionless approximation $\text{Rm} \ll 1$ is valid as the parameter regime is in the limit of low magnetic Reynolds number $\text{Rm} = \Omega r_i d / \eta$. This is because the fluid has very low magnetic Prandtl number $\text{Pm} = \nu / \eta \sim O(10^{-6})$ (eutectic alloy GaInSn⁵⁶) and only moderate Reynolds numbers $\text{Re} = \Omega r_i d / \nu \sim 10^3$ are considered giving rise to $\text{Rm} = \text{PmRe} \sim 10^{-3}$.

Decomposing the magnetic field as $\mathbf{B} = \hat{\mathbf{e}}_z + \text{Rm} \mathbf{b}$ and neglecting terms $O(\text{Rm})$, the Navier-Stokes and induction equations read

$$\partial_t \mathbf{v} + \text{Re} (\mathbf{v} \cdot \nabla) \mathbf{v} = -\nabla p + \nabla^2 \mathbf{v} + \text{Ha}^2 (\nabla \times \mathbf{b}) \times \hat{\mathbf{e}}_z, \quad (1)$$

$$0 = \nabla \times (\mathbf{v} \times \hat{\mathbf{e}}_z) + \nabla^2 \mathbf{b}, \quad (2)$$

$$\nabla \cdot \mathbf{v} = 0, \quad \nabla \cdot \mathbf{b} = 0. \quad (3)$$

In the framework of the inductionless approximation the MSC system is described in terms of three non-dimensional numbers: the Reynolds number, the Hartmann number and the aspect ratio

$$\text{Re} = \frac{\Omega r_i d}{\nu}, \quad \text{Ha} = \frac{B_0 d}{\sqrt{\mu_0 \rho \nu \eta}} = B_0 d \sqrt{\frac{\sigma}{\rho \nu}}, \quad \chi = \frac{r_i}{r_o}.$$

The boundary conditions for the velocity field are no-slip ($v_r = v_\theta = v_\varphi = 0$) at $r = r_o$ and constant rotation ($v_r = v_\theta = 0$, $v_\varphi = \sin \theta$) at $r = r_i$. As in previous studies (e.g., Ref. 29), and mimicking the experimental setting, insulating exterior regions are considered for the magnetic field.

The method to numerically solve the equations is described in Ref. 18 and references therein. The toroidal, Ψ , and poloidal, Φ , potentials are utilised to express the divergence-free velocity field

$$\mathbf{v} = \nabla \times (\Psi \mathbf{r}) + \nabla \times \nabla \times (\Phi \mathbf{r}). \quad (4)$$

The unknowns are expanded in spherical harmonics in the angular coordinates ($\mathbf{r} = r \hat{\mathbf{e}}_r$ is the position vector) and a collocation method on a Gauss–Lobatto mesh of N_r points is considered for the radial direction. More concretely, the solution vector $u = (\Psi, \Phi)$ (Eq. 4) is expanded in spherical harmonic series up to degree L_{\max} and order $M_{\max} = L_{\max}$ as

$$\Psi(t, r, \theta, \varphi) = \sum_{l=0}^{L_{\max}} \sum_{m=-l}^l \Psi_l^m(r, t) Y_l^m(\theta, \varphi), \quad (5)$$

$$\Phi(t, r, \theta, \varphi) = \sum_{l=0}^{L_{\max}} \sum_{m=-l}^l \Phi_l^m(r, t) Y_l^m(\theta, \varphi), \quad (6)$$

with $\Psi_l^{-m} = \overline{\Psi_l^m}$, $\Phi_l^{-m} = \overline{\Phi_l^m}$, $\Psi_0^0 = \Phi_0^0 = 0$ to uniquely determine the two scalar potentials, and $Y_l^m(\theta, \varphi) = P_l^m(\cos \theta) e^{im\varphi}$, P_l^m being the normalised associated Legendre functions of degree l and order m . The code is parallelised on the spectral and on the physical space by using OpenMP directives. Optimised libraries (FFTW3⁵²) for the FFTs in φ , and matrix-matrix products (dgemm GOTO⁵³) for the Legendre transforms in θ , are implemented for the computation of the nonlinear (advection) term.

High order implicit-explicit backward differentiation formulas (IMEX–BDF)⁵⁴ are used for the time integration. In the IMEX method we treat the nonlinear terms explicitly in order to avoid solving a nonlinear system of equations at each time step. The Lorenz force term in Eq. 1 is treated explicitly too, which may necessitate a reduced time step in comparison with an implicit treatment. However, this is not a serious issue when moderate Ha are considered,

as is the case for the present study. The use of *matrix-free* Krylov methods (GMRES⁵⁵ in our case) for the linear systems facilitates the implementation of a suitable order and time stepsize control for the time integration (see Ref. 54 for details of the implementation).

IV. RESULTS

The results presented in this section are based on direct numerical simulations for fixed $\chi = 0.5$, $\text{Re} = 10^3$ and control parameter $\text{Ha} \in [0, 6]$. According to table 1 of Ref. 18 this parameter regime is well resolved for $N_r = 40$ (number of radial collocation points) and $L_{\text{max}} = 84$ (spherical harmonics truncation parameter). From time to time, we increase the resolution to $N_r = 60$ and $L_{\text{max}} = 126$ to seek for discretisation errors which are below 1%.

The two previous studies (Refs. 18, 42) provided the bifurcation diagrams for rotating waves and modulated rotating waves including the above mentioned range of parameters. Specifically, branches of unstable/stable rotating waves with azimuthal symmetry $m = 2, 3, 4$ were computed¹⁸ and branches of MRW with azimuthal symmetries $m = 1, 2, 3$ were classified⁴² according to the established theory^{36,39}. Here, we start to compute the new flows using DNS with initial conditions built from RW or MRW previously obtained^{18,42}. By adding a small random perturbation to all the spherical harmonic amplitudes of these initial conditions, the model equations are time-stepped until an attractor is reached, that is, the flow is saturated and in a statistically steady state. To study the dependence of the flows on Ha we analyse time series of local (the radial velocity measured at a point inside the shell) or global physical properties such as the volume-averaged kinetic energy K . The latter is defined as

$$K = \frac{1}{2\mathcal{V}} \int_{\mathcal{V}} \mathbf{v} \cdot \mathbf{v} \, dv. \quad (7)$$

Concretely, we consider this volume integral for the non-axisymmetric component of the velocity field to define the non-axisymmetric K_{na} kinetic energy. It is based on the $m \neq 0$ modes of the spherical harmonic expansion of the potentials Ψ and Φ . This choice is motivated by the non-axisymmetric character of the radial jet instability, which is the focus of the present study. In addition, the previous volume integral can be computed for either the toroidal, $\nabla \times (\Psi \mathbf{r})$, or the poloidal, $\nabla \times \nabla \times (\Phi \mathbf{r})$, component of the velocity field, giving rise to either the toroidal, K^T , or the poloidal, K^P , kinetic energies.

For each wave number m in the spherical harmonic expansion (Eqs. 5-6), the instantana-

neous kinetic energy K_m is defined by only considering the spherical harmonic amplitudes ψ_l^m and ϕ_l^m with order m and degree $|m| \leq l \leq L_{\max}$. For each DNS, we search for m_{\max} with $\overline{K}_{m_{\max}} \geq \overline{K}_m$, $1 \leq m \leq L_{\max}$, being the time average. In our implementation an m -fold azimuthal symmetry for fixed $m = m_d$ can be imposed to obtain solutions with prescribed symmetry. This means that only the spherical harmonic amplitudes with azimuthal wave numbers being multiples of m_d are nonzero in Eqs. 5-6. We recall that a solution with m -fold azimuthal symmetry is unaffected by azimuthal rotations multiple of $2\pi/m$. Notice that if the azimuthal symmetry is $m = 1$ all the spherical harmonics amplitudes are considered. Flows with azimuthal symmetry $m = 1$ are considered stable if their time integration, after filtering initial transients, remains on the same attractor for sufficiently large time. In the case of flows obtained by constraining the azimuthal symmetry ($m = 2$ or $m = 3$) their stability is assessed by adding an $m = 1$ random perturbation. They are considered unstable if the $m = 1$ perturbation grows in time. By means of time spectrum analysis and Poincaré sections we infer the quasiperiodic or chaotic character of the DNS.

A. Type of flows with $\text{Ha} < 6$

Because the basic flow is axisymmetric ($m = 0$ azimuthal symmetry) the volume-averaged nonaxisymmetric ($m \neq 0$) component of the kinetic energy, K_{na} , is used as a proxy for the bifurcation diagrams of the time dependent flows presented in this section. Concretely, the time average of the time series of K_{na} for each computed solution is considered. In addition, we display the maximum and minimum values of the time series of K_{na} to estimate the amplitude of fluctuations. For this purpose, sufficiently large time series (more than 10 dimensionless time units, i.e. viscous time-scales) have to be obtained. This is especially true close to bifurcation points where long initial transients are expected.

Figure 2 displays the time average \overline{K}_{na} versus the Hartmann number Ha for weakly magnetised flows corresponding to the radial jet instability. Several branches are shown and two integers –the azimuthal symmetry m and most energetic azimuthal wave number m_{\max} – are used to label them. As usual, stable/unstable motions are marked with different line type (solid/dashed). The branches shown in the figure can be classified as four classes of flows: flows with $m = 1$ and $m_{\max} = 3$, flows with $m = 1$ and $m_{\max} = 2$, flows with $m = 3$ and flows with $m = 2$.

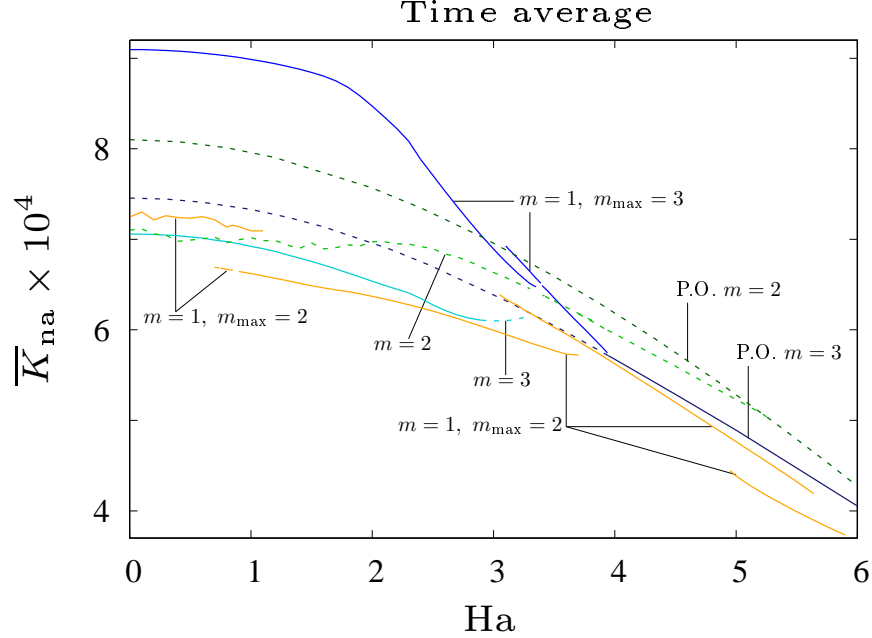


FIG. 2. Bifurcation diagrams of the nonaxisymmetric ($m \neq 0$) time and volume averaged kinetic energy \overline{K}_{na} versus the Hartmann number Ha for weakly magnetised flows corresponding to the equatorially asymmetric radial jet instability (color online). The azimuthal symmetry m and most energetic azimuthal wave number m_{max} are displayed on each branch. Four general classes of complex flows are shown: flows with $m = 1$ and $m_{max} = 3$ (blue), flows with $m = 1$ and $m_{max} = 2$ (orange), flows with $m = 3$ (turquoise) and flows with $m = 2$ (green). Branches of periodic orbits with $m = 2, 3$ are displayed as well. Solid/dashed lines mean stable/unstable flows.

For each of the two latter cases ($m = 2, 3$) a branch of rotating waves (periodic orbits labelled with P.O.), as previously computed in Ref. 18, is shown. Hopf bifurcations along these P.O. branches give rise to modulated rotating waves MRW, with $m = 1$ and $m_{max} = 3$, $m = 3$ or $m = 2$, whose spatio-temporal symmetry was analysed in Ref. 42. The branches of complex flows corresponding to $m = 1$ and $m_{max} = 2$ are however not directly connected with those of the P.O. For this class of flows ($m = 1$ and $m_{max} = 2$) some MRW were studied in Ref. 42 as well. The MRW of Ref. 42 have been described for $Ha > 2.5$, while in Fig. 2 their branches are extended down to $Ha = 0$. In addition, Fig. 2 contains other branches of waves and chaotic flows not previously found in Ref. 42.

In order to simplify the exposition of the description of the flows displayed in Fig. 2 the class of flows with $m = 1$ and $m_{max} = 3$, and the class of flows with $m = 3$ can be joined

into the class $m_{\max} = 3$. Then, three different classes (i) $m_{\max} = 3$ (ii) $m = 1$ and $m_{\max} = 2$, and (iii) $m = 2$, are obtained. The three following sections describe these classes of flows, and the bifurcations among them.

B. Flows with $m_{\max} = 3$

Figure 3(a) details the type of temporal dependence detected on each of the branches shown in Fig. 2 corresponding to the class of flows with $m_{\max} = 3$. The maximum (thick line) and minimum (thin line) values of the volume-averaged nonaxisymmetric ($m \neq 0$) kinetic energy, for three different branches with $m = 1$ -fold azimuthal symmetry (Branch 1 and Branch 2) and with $m = 3$ -fold azimuthal symmetry (Branch 3), are plotted versus Ha . Solutions of Branch 1, and those of Branch 3 for $Ha \in [2.5, 3.25]$, were studied previously in Ref. 42. We recall that both branches arise, due to a Hopf bifurcation on the branch of RW (periodic orbits, P.O., solid line), giving rise to MRW which are invariant tori with two frequencies (2T, dashed line). As noticed in Ref. 42 the volume-averaged properties of MRW of Branch 1 have very small oscillations and thus their maximum and minimum values are almost the same (see Fig. 3(a)). This does not occur for MRW of Branch 3, as it is usually expected for these type of waves⁴⁹.

By decreasing Ha from $Ha = 2.5$ and taking initial conditions on the MRW (2T) of Branch 3 a period doubling bifurcation (labelled P.D., dashed-dotted line) is detected and the branch extends down to $Ha = 0$. Similarly, decreasing Ha but from MRW of Branch 1, a branch of invariant tori with three frequencies (3T, dashed-double-dotted line) is obtained at around $Ha \approx 3.4$ as a result of a Hopf bifurcation. By taking a 3T initial condition of Branch 1 with $Ha = 3.1$ and decreasing Ha down $Ha = 3$ a new branch, called Branch 2, is found. The type of solutions is 3T and hysteresis behaviour is observed as this new branch can be continued up to $Ha \approx 3.35$. A subcritical pitchfork bifurcation, together with a re-stabilisation and possible folding, may be the origin of this new branch as we will argue later on the text. By extending Branch 2 from $Ha = 3$ down to $Ha = 0$ a 2T solution, and a 3T solution, branches are found. In other words, we have found a branch of 2T solutions connecting two branches of 3T solutions.

Figure 3(b,c,d) display the result of the frequency analysis in Hz. As we solve dimensionless equations, the frequencies should be translated in Hz. We assume the kinematic

Flows with $m_{\max} = 3$

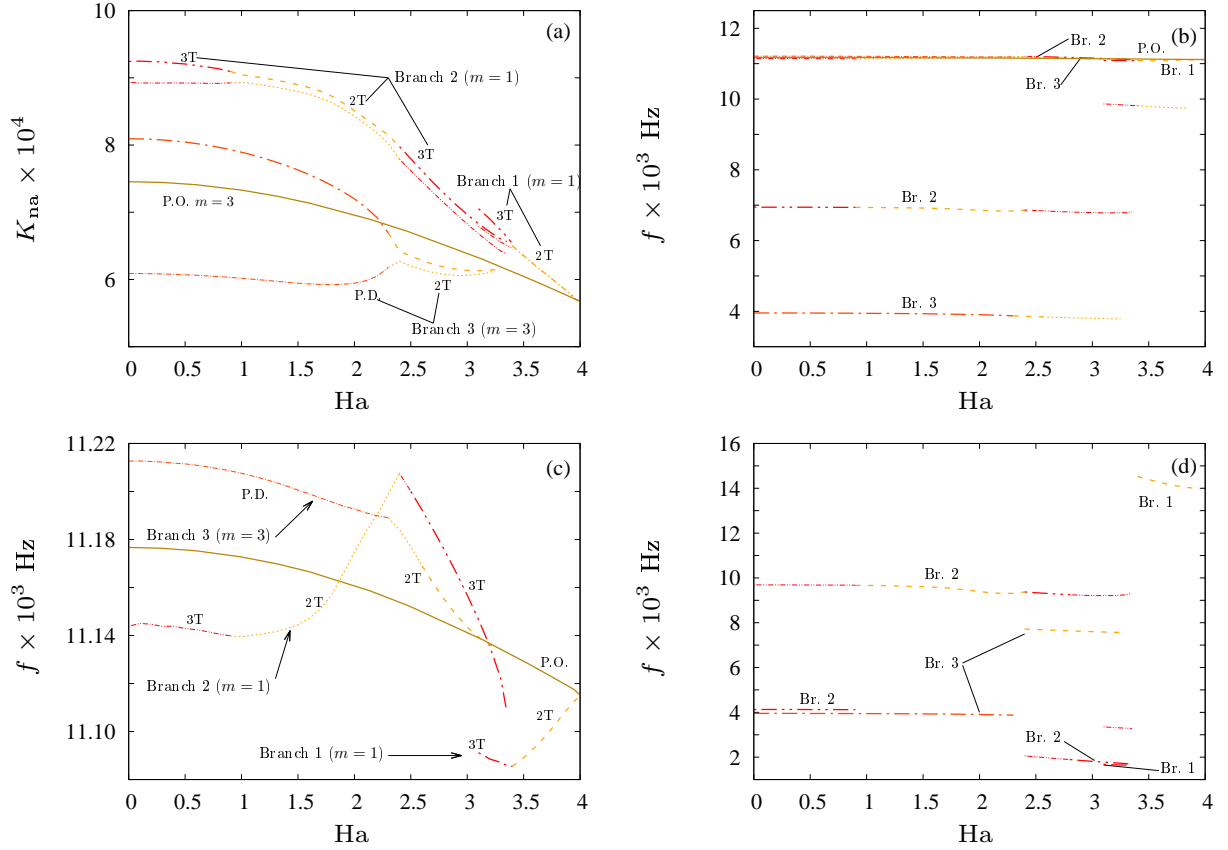


FIG. 3. Flows with $m_{\max} = 3$ (either with $m = 1$ or $m = 3$). (a) Maximum (thick line) and minimum (thin line) of K_{na} . (b) 1st (thick line) and 2nd (thin line) dominant frequencies (the two having largest amplitude) of the flow. (c) Detail of (b) showing the frequencies in the range of ≈ 0.011 Hz. (d) 1st (thick line) and 2nd (thin line) dominant frequencies of the volume-averaged kinetic energy. The type of solutions –periodic orbit (P.O., solid line), invariant tori (2T, dashed line), invariant tori with period doubling (P.D., dashed-dotted line), and invariant tori with three frequencies (3T, dashed-double-dotted line)– is marked on each branch.

viscosity of the eutectic alloy $\text{Ga}^{67}\text{In}^{20.5}\text{Sn}^{12.5}$ may be approximated by $\nu = 3.4 \times 10^{-3} \text{cm}^2 \text{s}^{-1}$ (see Ref. 56). Together with the geometric setup of the Hedgehog experiment, with $r_o = 9$ cm and $r_i = 4.5$ cm, the dimensional value for the frequencies computed in this study is $f = f^* \nu / d^2 = 1.7 \times 10^{-3} f^*$ Hz, f^* being a dimensionless frequency. Figure 3(b) (and its detail (c)) shows the 1st (thick line) and 2nd (thin line) dominant Laskar’s⁵⁰ frequencies (the two frequencies having largest amplitude). They are computed from the time series of the

radial velocity picked up at the point $(r_i + 0.5d, \pi/8, 0)$ for solutions of the same branches of Fig. 3(a).

Figure 3(b) evidences an interchange of the two dominant frequencies on all the main branches (Branch 1, 2, and 3) as Ha is decreased. We have to note however that the amplitudes of both frequencies remain similar. Because the 1st and 2nd dominant frequencies are not related by an integer constant, they are independent and thus describe the temporal scales (in Hz) expected for flows at this range of parameters. As seen in Fig 3(b) all the branches have one frequency in the range $[11.08, 11.22]$ which in turn is quite similar to the unique frequency along the branch of P.O., which corresponds to the rotating frequency of the waves³⁶. A detail of this is shown in Fig 3(c) where the transitions among the different type of flows can be clearly identified.

Figure 3(d) is as Fig. 3(b), but for the time series of the volume-averaged kinetic energy. Because it is a volume (and thus azimuthally) averaged quantity, the drifting frequency of the flow shown in Figs. 3(b,c) does not appear and the frequencies correspond exclusively to those driving the modulation. This means in turn that 2T solutions exhibit only one frequency and 3T solutions exhibit 2 frequencies. From Fig. 3(d) it becomes clear that on Branch 3 a period doubling bifurcation occurs around $Ha = 2.3$. Moreover, close to $Ha = 3.35$ the frequencies of the 3T solutions at Branch 1 and at Branch 2 are very similar as it is the case for the drift frequency shown in Fig. 3(c). This provides some evidence that both branches are related and, as commented earlier, the relation could be a pitchfork bifurcation. The study of the main frequencies, and thus the temporal scales of the flow, is relevant for future comparisons with the HEDGEHOG experiment¹⁶.

The analysis of the two main frequencies of the flow does not provide a complete description of the time dependence as the time spectrum usually consists of many of them. We now confirm that for a 2T (3T) solution all frequencies present in the spectrum have to be an integer linear combination of two (three) fundamental frequencies^{50,57}. The Poincaré section helps to rigorously validate the existence of 2T solution from a time series of a dynamical system. The Poincaré section constructed from a periodic time series is a point whereas it corresponds to a closed curve if the time series involves two fundamental frequencies. In our case, considering the time series of volume-averaged quantities (and thus eliminating one frequency of the system) will help to identify 3T solutions as its Poincaré section will correspond to a closed curve.

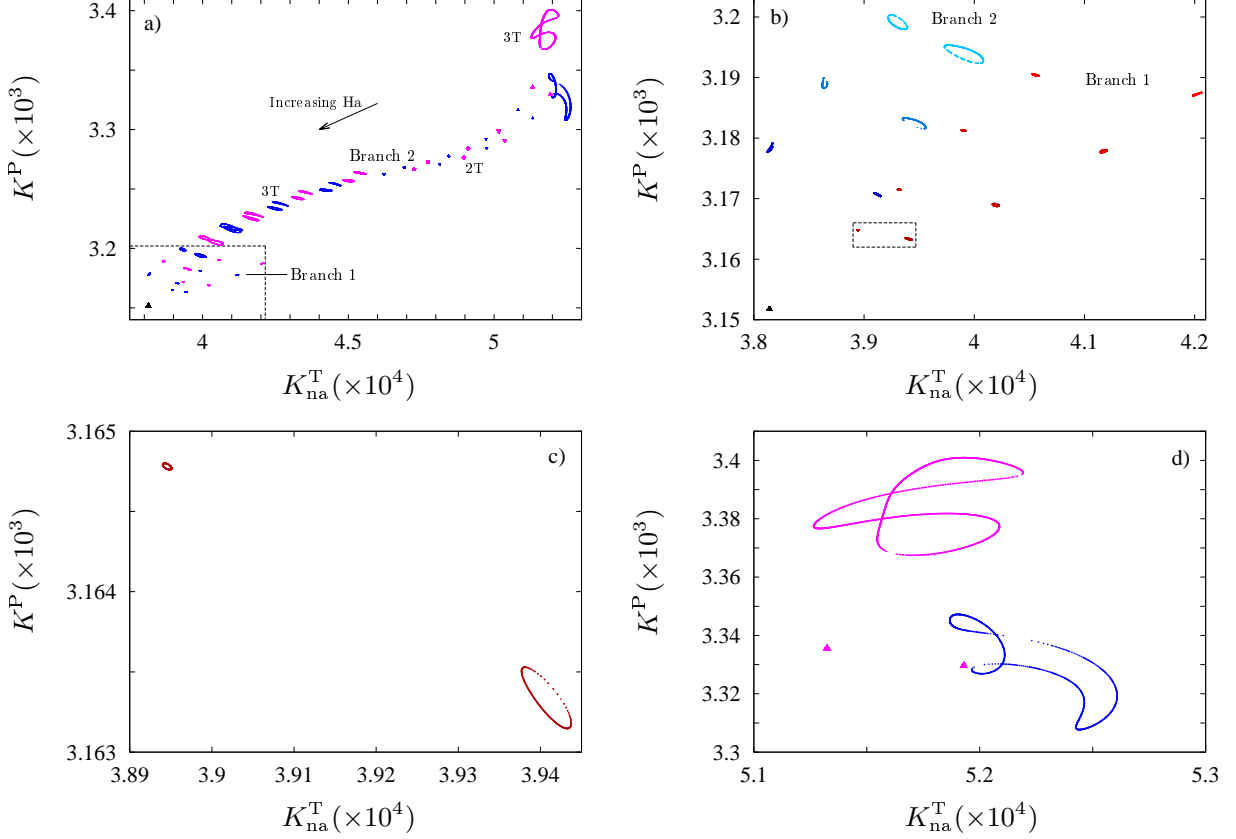


FIG. 4. Flows with $m = 1$, $m_{\max} = 3$: Poincaré sections defined by the constraint $K(t) = \bar{K}$, K being the volume-averaged kinetic energy and \bar{K} its time average. The volume-averaged poloidal kinetic energy K^P is displayed versus the volume-averaged toroidal nonaxisymmetric energy K_{na}^T . (a) Sequence of invariant tori with two (2T, points) and three (3T, closed curves) frequencies for Branches 1 and 2. The Hartmann numbers are $Ha = 3.1, 3.2, 3.3, 3.37, 3.5$ for Branch 1 and $Ha = 0, 0.7, 1.1, 1.5, 1.8, 1.9, 2, 2.1, 2.2, 2.3, 2.4, 2.5, 2.6, 2.7, 2.8, 2.9, 3., 3.1, 3.2, 3.3$ for branch 2. The solution on the left bottom corner corresponds to a 2T solution at $Ha = 3.5$. (b) Detail of (a) showing the transition between 2T solution (point on the left bottom corner) and the two branches of 3T solutions. (c) Detail of (b) displaying a 3T solution on branch 1 very close to the bifurcation. (d) Detail of the Poincaré sections of complex 3T attractors found at $Ha = 0$ and $Ha = 0.7$ and those of a 2T solution at $Ha = 1.1$.

Figure 4 displays the (two) Poincaré sections defined by the constraint $K(t) = \bar{K}$, K being the volume-averaged kinetic energy and \bar{K} its time average. The volume-averaged poloidal kinetic energy K^P is plotted versus the volume-averaged toroidal nonaxisymmetric energy

K_{na}^T . The figure illustrates the bifurcation scenario on Branch 1 and 2. For each solution of Fig. 4(a) the two Poincaré sections are very close with their Hartmann numbers increasing from the top right corner following the arrow. For Branch 1 $Ha \in [3.1, 3.5]$, while for Branch 2 $Ha \in [0, 3.3]$. The triangle on the left bottom corner corresponds to a 2T solution (a point) at $Ha = 3.5$ and by decreasing Ha the two branches of 3T solutions (Branch 1 and 2) can be identified as closed curves (see details of Fig. 4(b,c)). As commented before, on Branch 2 there is a branch of 2T solutions (points on the right part of Fig. 4(a)) connecting the two branches of 3T solutions. The Poincaré sections appearing at the right top corner (see detail Fig. 4(d)) correspond to complex 3T attractors found at $Ha = 0$ and $Ha = 0.7$.

The solutions of Branch 1 and 2 are stable since they are obtained by means of DNS without symmetry assumptions. Solutions on Branch 3, obtained when imposing an $m = 3$ symmetry, are unstable for $Ha \in [2.9, 3.25]$ and they are stable for $Ha < 2.9$. The stability of these solutions is assessed by analysing the growth or decay of a random perturbation with azimuthal symmetry $m = 1$. The interval of Hartmann numbers for the stability of each type of temporal dependence (P.O., 2T, and 3T) on each branch shown in Fig. 3(a) is provided in Table I.

TABLE I. Range of Hartmann numbers for the stability of the different types of temporal dependence along the different branches (Branch 1, 2 and 3) for flows with $m_{\max} = 3$. The interval of definition of the nonaxisymmetric radial jet instability is $Ha \in [0, Ha_c)$ with $Ha_c = 12.2$ being the critical Hartmann number¹⁷.

type of flow	Branch 1	Branch 2	Branch 3
P.O.	(3.95, 12.2)		
2T	(3.39, 3.95)	(0.85, 2.45)	[0, 2.9)
3T	(3.05, 3.39)	[0, 0.85) \cup (2.45, 3.37)	

C. Flows with $m = 1$, $m_{\max} = 2$

This section focuses on the analysis of the class of flows with $m = 1$, $m_{\max} = 2$, previously shown in Fig. 2. Figure 5, displaying the same quantities as Fig. 3, summarises this analysis. Several isolated branches (Branch 1, 2, 3, and 4) are displayed and the flow on each branch

can exhibit different types of temporal dependence. On Branch 1 only invariant 2T flows are obtained (right bottom corner, Fig. 5) while Branch 4 is formed only by strongly oscillatory chaotic flows. Branches 2 and 3 contain 2T solutions as well as a small interval of 3T solutions.

The curves of 2T solutions in the Branches 1 and 2 were studied previously in Ref. 42 and the spatio-temporal symmetries of the solutions were determined. These branches were obtained by taking initial conditions, and perturbing them, on the branch of rotating waves (P.O.) with $m = 2$ -fold azimuthal symmetry first computed in Ref. 18. By slightly decreasing Ha and taking initial conditions on the left part of the curve of 2T solutions on Branch 2 (at around $Ha \approx 3.6$) a branch of 3T solutions is found. By further decrease of Ha , and similarly to what occurred on Branch 1 for flows with $m_{\max} = 3$ (previous section), the 3T solutions on Branch 2 give rise to 2T solution on the new Branch 3 and a hysteretic behaviour is found. This happens at around $Ha \approx 3$. As commented in the previous section, this behaviour may be associated to a subcritical pitchfork bifurcation on Branch 2.

By decreasing Ha the curve of 2T solutions on Branch 3 extends down to $Ha \approx 0.9$ and undergoes a period doubling bifurcation followed by a Hopf bifurcation giving rise to 3T solutions. This occurs in a very narrow interval $Ha \in (0.7, 0.9)$. For $Ha < 0.7$ the only flows found are the chaotic ones of Branch 4. Again, hysteresis occurs and the presence of chaotic flows extends up to $Ha \approx 1$. The curves of the maximum and minimum volume-averaged nonaxisymmetric ($m \neq 0$) kinetic energy of flows belonging to Branch 4 (shown in Fig. 5) are clearly non-smooth, which is a sign of the chaotic behaviour of the solutions. Further confirmation of this chaotic time dependence will be provided in the next section when comparing Branch 4 with the chaotic flows found when the azimuthal symmetry is $m = 2$.

Figures 5(b,c,d) correspond to the frequency analysis of regular solutions, i. e. of Branches 1, 2, and 3. Similarly as described in the previous section, for flows with $m_{\max} = 3$, the main frequency is very close to the drifting frequency (around 7 mHz) of the rotating waves (P.O.) (see Fig. 5(b) and its detail (c)). The second dominant frequency seen in Fig. 5(b) is related to the frequency giving rise to the quasiperiodic behaviour, physically corresponding to the modulation of the wave, i. e., to the oscillation of volume averaged properties. As displayed in Fig. 5(d), the latter oscillations have large temporal time scales when compared with the time scales associated with the azimuthal drifting of the wave. Notice that for the invariant tori with period doubling P.O. of Branch 3 the main frequency and the halved frequency are

Flows with $m = 1$, $m_{\max} = 2$

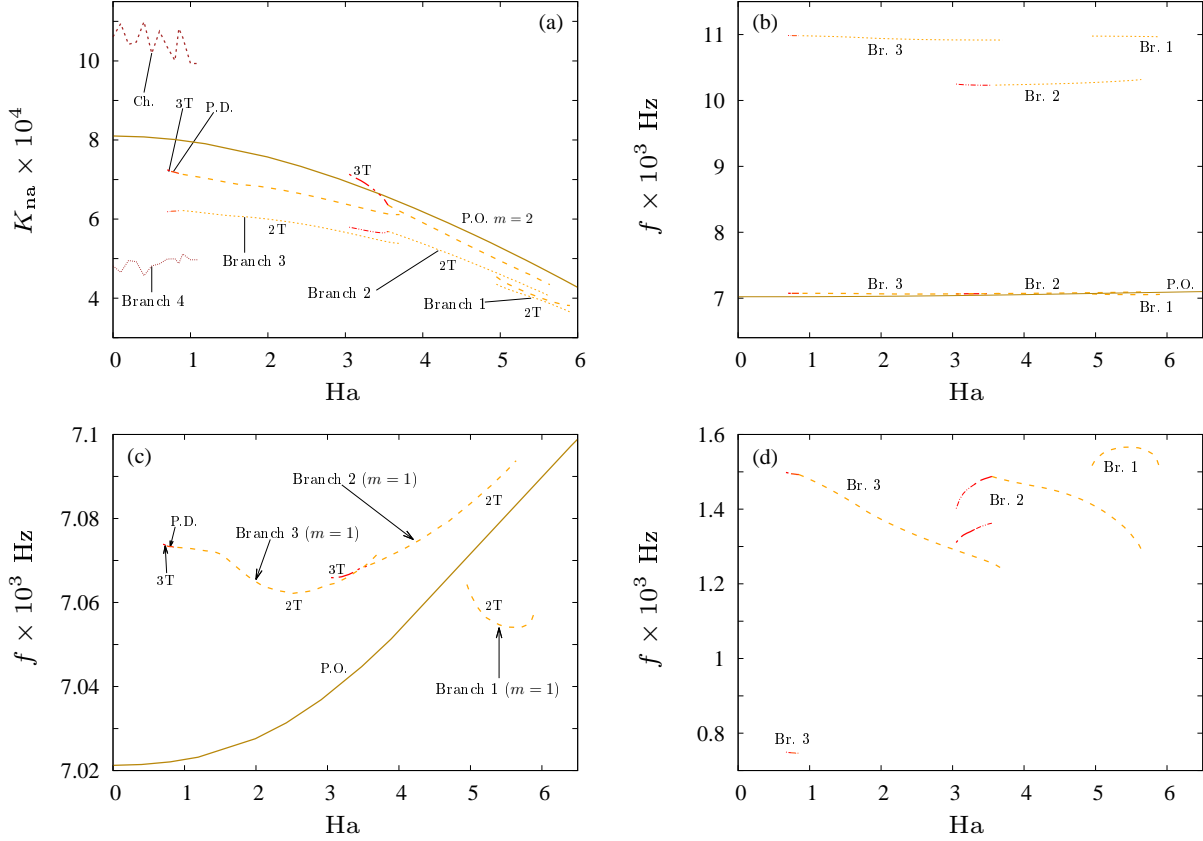


FIG. 5. Flows with $m = 1$ and $m_{\max} = 2$. (a) Maximum (thick line) and minimum (thin line) of K_{na} . (b) 1st (thick line) and 2nd (thin line) dominant frequencies (the two having largest amplitude) of the flow. (c) Detail of (b) showing the frequencies in the range of ≈ 0.007 Hz. (d) 1st (thick line) and 2nd (thin line) dominant frequencies of the volume-averaged kinetic energy. The type of solutions –periodic orbit (P.O., solid line), invariant tori (2T, dashed line), invariant tori with period doubling (P.D., dashed-dotted line), invariant tori with three frequencies (3T, dashed-double-dotted line), and chaotic flows (Ch., dotted line)– is marked on each branch.

both shown on the left part of Fig. 5(d).

Several Poincaré sections are displayed on Fig. 6 to demonstrate the type of time dependence of flows with $m = 1$ and $m_{\max} = 2$. On Fig. 6(a) the Poincaré sections are defined by $v_r(r_1, \pi/8, 0) = -6 \times 10^{-2}$ whereas on Fig. 6(b) the sections are defined by the constraint $K(t) = \bar{K}$, K being the volume-averaged kinetic energy and \bar{K} its time average. As commented previously, considering a volume averaged quantity (such as \bar{K}) in the definition

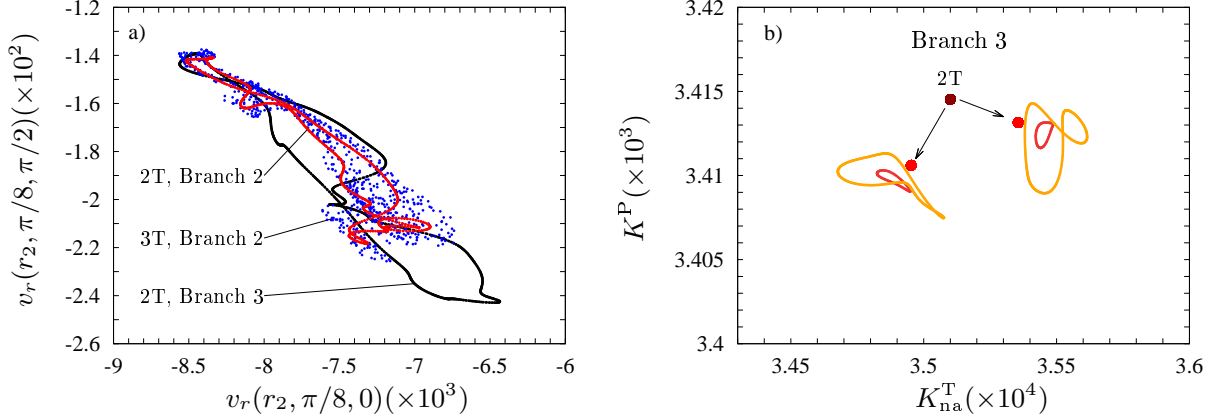


FIG. 6. Flows with $m = 1$, $m_{\max} = 2$ (a) Poincaré sections defined by $v_r(r_1, \pi/8, 0) = -6 \times 10^{-2}$. The radial positions are $r_1 = r_i + 0.5d$ and $r_2 = r_i + 0.85d$. Invariant tori with two frequencies (2T) of the 2nd and 3rd branches at $\text{Ha} = 3.7$ as well as an invariant torus with 3 frequencies (3T) of the 2nd branch at $\text{Ha} = 3.5$ are displayed. (b) Poincaré sections defined by the constraint $K(t) = \bar{K}$, K being the volume-averaged kinetic energy and \bar{K} its time average. The volume-averaged poloidal kinetic energy K^P is displayed versus the volume-averaged toroidal nonaxisymmetric energy K_{na}^T . On the 3rd branch, invariant tori with two frequencies at $\text{Ha} = 1$ and at $\text{Ha} = 0.8$ are marked with large points. Notice that from $\text{Ha} = 1$ to $\text{Ha} = 0.8$ a period doubling bifurcation (see arrows) has occurred. For smaller Ha a transition to 3 frequency invariant tori (small red at $\text{Ha} = 0.74$ and large orange at $\text{Ha} = 0.7$ closed curves) occurs.

of the Poincaré section allows to identify 3 frequency solutions (3T), as they correspond to closed curves (the drifting frequency is removed by volume averaging).

Figure 6(a) displays the sections of three different flows: 2T solution ($\text{Ha} = 3.7$) and 3T solution ($\text{Ha} = 3.5$) on Branch 2 and a 2T solution ($\text{Ha} = 3.7$) on Branch 3. As the radial velocity v_r is not a volume-averaged quantity, the 2T solutions correspond to closed curves and the 3T solutions correspond to the cloud of points. The shape of the curves is indeed characteristic of complex 2T attractors. Comparing these two curves at the same $\text{Ha} = 3.7$ helps to compare Branch 2 with Branch 3. Notice that oscillations of v_r are more developed on Branch 3 as the Poincaré section encloses a larger area. Between $\text{Ha} = 1$ and $\text{Ha} = 0.8$ a period doubling of 2T flows on Branch 3 can be identified from Fig. 6(b). At $\text{Ha} = 1$ the Poincaré section is a single point whereas at $\text{Ha} = 0.8$ it consists of two points, i.e. it has doubled the period. In addition, at $\text{Ha} = 0.74$ and $\text{Ha} = 0.7$ a new independent frequency

TABLE II. Range of Hartmann numbers for the stability of the different types of temporal dependence along the different branches for flows with $m = 1$ and $m_{\max} = 2$. The interval of definition of the nonaxisymmetric radial jet instability is $\text{Ha} \in [0, \text{Ha}_c)$ with $\text{Ha}_c = 12.2$ being the critical Hartmann number¹⁷.

type of flow	Branch 1	Branch 2	Branch 3	Branch 4
2T	[4.95, 5.9]	[3.55, 5.64]	[0.75, 3.7]	
3T		[3.05, 3.55]	[0.7, 0.74]	
Ch.				[0, 1]

appears -by means of a Hopf bifurcation- giving rise to 3T solutions whose Poincaré sections of volume-averaged quantities become closed curves.

With the exception of the branch of P.O., all flows described in this section are stable. The interval of Hartmann numbers for the stability of each type of temporal dependence (2T, 3T, and Ch.) on each branch shown in Fig. 5(a) is provided in Table II.

D. Flows with $m = 2$

In this section the class of flows with $m = 2$, first displayed on Fig. 2 and obtained imposing $m = 2$ -fold azimuthal symmetry on the DNS, is investigated. Figure 7(a) displays the maximum and minimum values of the volume-averaged nonaxisymmetric $m \neq 0$ kinetic energy of the different types of flows. According to Refs. 18, 42 a branch of 2T solutions is born at $\text{Ha} \approx 5.25$ through a Hopf bifurcation on the unstable branch of periodic orbits P.O.. This branch of 2T solutions extends down to $\text{Ha} \approx 3.94$ where a tertiary Hopf bifurcation gives rise to a new branch of 3T solutions. A rich variety of flow types is found by decreasing $\text{Ha} \in [3, 4]$ from this point. First, an interval of frequency locking (F.L.) –a parameter region where the ratio of two fundamental frequencies becomes a constant rational number (see Ref. 58 for instance)– on a branch of 3T solutions is found. This is followed by a doubling period cascade giving rise to chaotic flows at the smallest Ha.

The frequency analysis for the radial velocity summarised in Fig. 7(b,c,d) provides further evidence for the above mentioned scenario. Panel (b) indeed confirms what was observed in Secs. IV B-IV C: The main frequency of the flow is quite constant and remains very close

Flows with $m = 2$

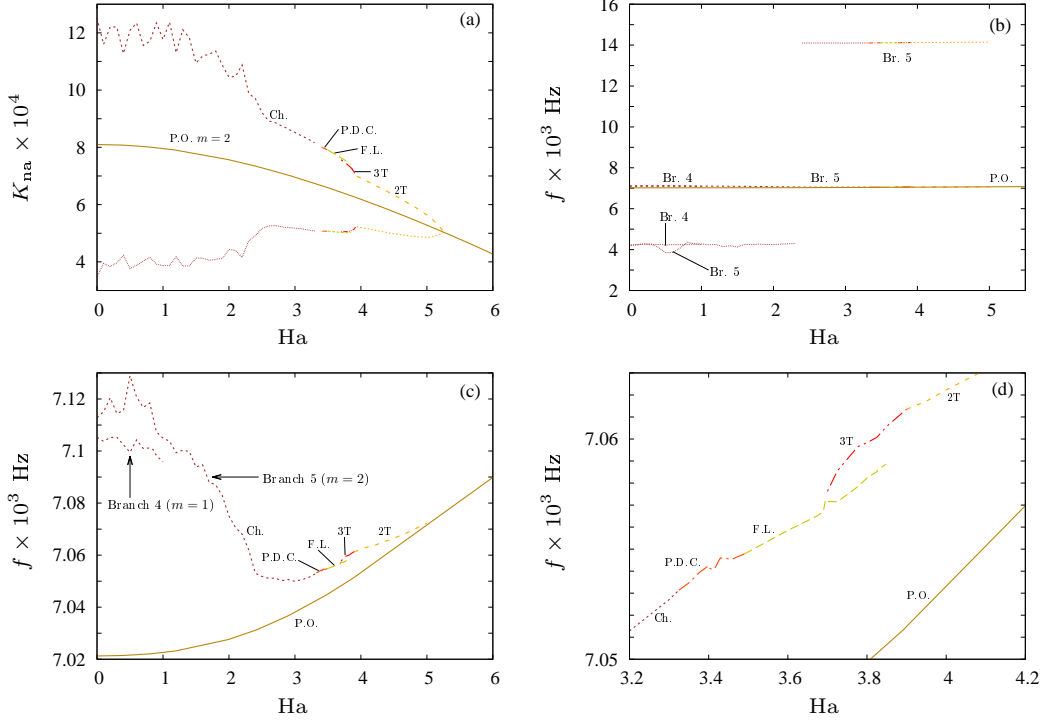


FIG. 7. Flows with $m = 2$. (a) Maximum (thick line) and minimum (thin line) of K_{na} . (b) 1st (thick line) and 2nd (thin line) dominant frequencies (the two having largest amplitude) of the flow. (c) Detail of (b) showing the frequencies in the range of ≈ 0.007 Hz. (d) 1st (thick line) and 2nd (thin line) dominant frequencies of the volume-averaged kinetic energy. The type of solutions – periodic orbit (P.O., solid line), invariant tori (2T, dashed line), invariant tori with period doubling (P.D., dashed-dotted line), invariant tori with three frequencies (3T, dashed-double-dotted line), and chaotic flows (Ch., dotted line)– is marked on each branch.

to the one corresponding to the unstable rotating waves with $m = 2$ at the same range of parameters. The label Br. 5 on Fig. 7(b) (and on its detail, Fig. 7(c)) refers to Branch 5, which is the branch corresponding to $m = 2$ displayed on Fig. 7(a). The label Br. 4 corresponds to Branch 4, a branch of chaotic flows with $m = 1$, $m_{\max} = 2$ already described in Sec. IV C. As happens for the nonaxisymmetric kinetic energy, see Fig. 2 and compare Fig. 5(a) with Fig. 7(a), the values of the 1st and 2nd frequencies are very close giving evidence of the relation between Branch 4 and Branch 5. Solutions lying on the latter branch seem to be the projection onto the $m = 2$ subspace of the corresponding solution

with $m = 1$, as this is slightly more energetic (see Fig. 2) because it contains more spherical harmonics.

Figure 7(d) details the bifurcation scenario in the interval $\text{Ha} \in [3.2, 4.2]$. As commented before, an interval of frequency locking on a branch of 3T solutions is found for $\text{Ha} \in [3.5, 3.8]$. In this range the ratio is $f_1/f_2 = 1.5 \pm 3 \times 10^{-3}$, f_1, f_2 being the 1st and 2nd dominant Laskar⁵⁰ frequencies of the volume averaged kinetic energy spectrum. In a narrow interval around $\text{Ha} > 3.4$ a sequence of period doubling bifurcations is found. The estimated critical parameters, Ha_i ($i = 1, \dots, 4$), are $\text{Ha}_1 = 3.491$, $\text{Ha}_2 = 3.423$, $\text{Ha}_3 = 3.4073$, and $\text{Ha}_4 = 3.4039$. The Feigenbaum iterates are $\delta_1 = 4.33$ and $\delta_2 = 4.62$ (with the definition $\delta_i = (\text{Ha}_{i+1} - \text{Ha}_i)/(\text{Ha}_{i+2} - \text{Ha}_{i+1})$), in good agreement with the Feigenbaum constant $\delta = 4.6692$. A period doubling cascade was also found in Ref. 59 when restricting the azimuthal symmetry in the context of thermal convection in rotating spherical shells.

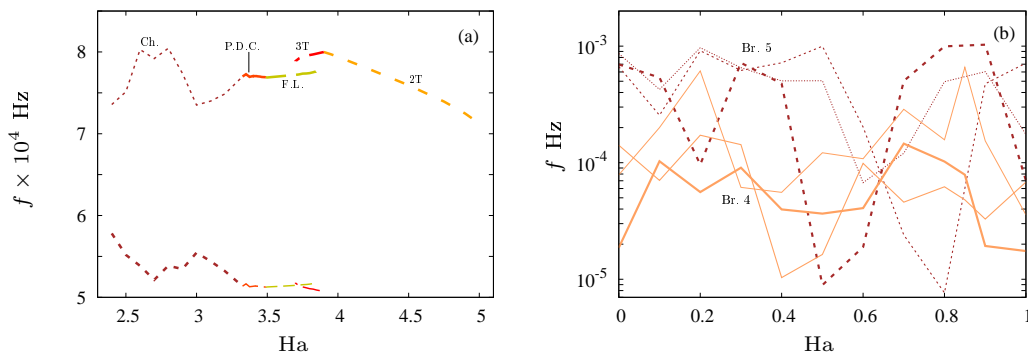


FIG. 8. Two different branches with $m = 1$ -fold azimuthal symmetry (Branch 4) and with $m = 2$ -fold azimuthal symmetry (Branch 5) are shown. (a) the 1st (thick line) and 2nd (thin line) dominant (those of largest amplitude) frequencies of a time series of the volume-averaged kinetic energy for solutions of Branch 5. (b) As (a) but including the chaotic solutions with $m = 1$ -fold azimuthal symmetry (Branch 4) in the range $\text{Ha} \in [0, 1]$. The type of solutions –invariant tori with two frequencies (2T, dashed line), invariant tori with three frequencies (3T, dashed-double-dotted line), invariant tori with two frequencies coming from period doubling cascade (P.D.C., dashed-dotted), chaotic flows (Ch., dotted line) and periodic orbit (P.O., solid line) – is marked on each branch. For this class of flows an interval of frequency locking on a branch of 3T solutions is obtained (F.L., long-dashed line).

Figure 8(a,b) displays the main frequencies associated with the time series of the volume-

averaged kinetic energy. It supports the visualisation of long time scales of the flow evolution (with frequencies less than a mHz) associated with the modulation. Figure 8(a) evidences the region of frequency locking as the curves for the 1st and 2nd frequencies (thick/thin line) have the same shape and we have checked that they differ only by a constant (3/2) factor. Figure 8(b) displays the three main frequencies only for the chaotic flows of branches 4 and 5 in the range $\text{Ha} \in [0, 1]$. The chaotic behaviour of solutions on each branch gives rise to sharp changes as Ha is varied. All the frequencies are very small giving rise to time scales up to 10^5 seconds, i. e. a whole day. We note that both, Branch 4 and 5, exhibit the same behaviour with Ha providing further confirmation of the relation among both branches.

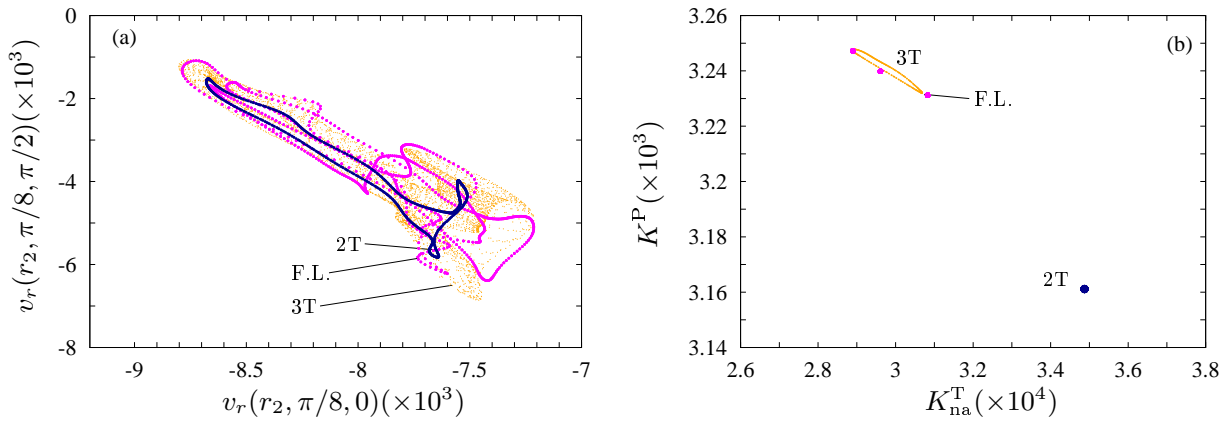


FIG. 9. Flows with $m = 2$ (a) Poincaré sections defined by $v_r(r_1, \pi/8, 0) = -6 \times 10^{-2}$. The radial positions are $r_1 = r_i + 0.5d$ and $r_2 = r_i + 0.85d$. An invariant torus with two frequencies (2T) at $\text{Ha} = 4$ as well as an invariant torus with 3 frequencies (3T) and a resonant (frequency locked) 3T solution at $\text{Ha} = 3.8$ are displayed. (b) Poincaré sections defined by the constraint $K(t) = \bar{K}$, with K being the volume-averaged kinetic energy and \bar{K} its time average. The volume-averaged poloidal kinetic energy K^P is displayed versus the volume-averaged toroidal nonaxisymmetric energy K_{na}^T . The invariant torus with two frequencies at $\text{Ha} = 4$ is marked with a large point. The closed curve corresponds to the 3T solution at $\text{Ha} = 3.8$. The set of three points lying on the curve correspond to the resonant 3T solution at $\text{Ha} = 3.8$.

Again, confirmation of the bifurcation scenario is provided by the inspection of the Poincaré sections. Figure 9(a) provides a picture of the section, defined in terms of the radial velocity, of a 3T solution (cloud of dots) and the corresponding section of a frequency locking solution (closed larger curve) at $\text{Ha} = 3.8$. Both sections are similar (same elonga-

tion and similar occupation of area) with that of the 2T solution at $Ha = 4$, meaning that the three solutions are related as they arise at different bifurcations on the same branch. If the volume averaged kinetic energy is used to define the Poincaré section (Fig. 9(b)) the situation is even more clear since the 3T solution is a closed curve and the frequency locked 3T solution is a set of 3 points.

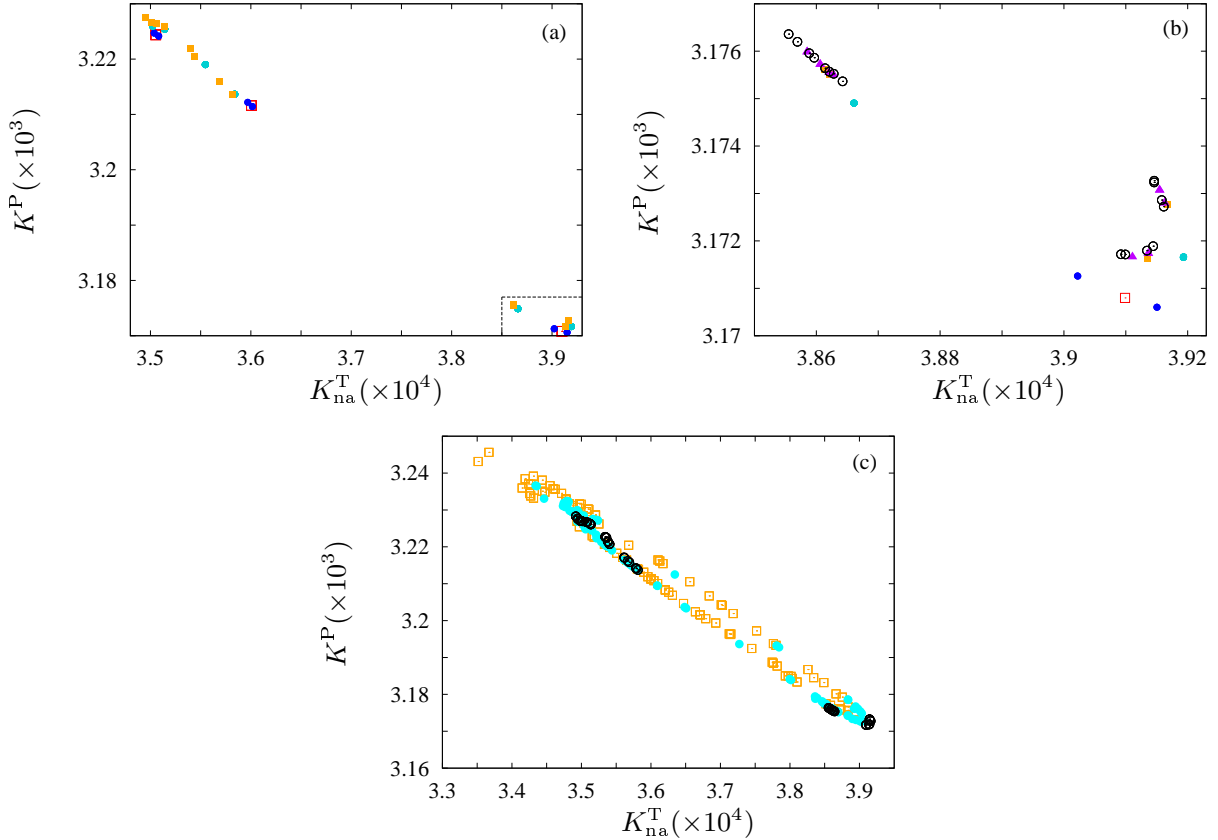


FIG. 10. Period doubling cascade with $m = 2$. The Poincaré sections are as in Fig. 4. (a) The set of three points (open squares) correspond to a resonant 3T solution at $Ha = 3.4925$. At $Ha = 3.49$ and $Ha = 3.43$ the Poincaré sections contain 6 points (full circles). At $Ha = 3.41$ the Poincaré section contains 12 points (full squares). (b) Detail of (a) showing additional Poincaré sections at $Ha = 3.406$ (24 points, full triangles) and at $Ha = 3.403$ (48 points, open circles). (c) Period doubling flow at $Ha = 3.403$ (48 points, open circles) and chaotic flows at $Ha = 3.35$ (full circles) and $Ha = 3.3$ (open squares).

Figure 10 displays the Poincaré sections defined in terms of volume averaged properties (see figure caption) of flows undergoing a sequence of period doubling bifurcations. These Poincaré sections are again quite useful to identify the period doubling cascade, on a branch

of 3T solutions with frequency locking, as the number of points is doubled at each bifurcation. The first and second period doubling bifurcations are visualised on Fig. 10(a). The set of 3 points at $Ha = 3.4925$ (open squares) become 6 points (full circles) at $Ha = 3.49, 3.43$ and 12 points (full squares) at $Ha = 3.41$. Figure 10(b) deepens this investigation providing the sections for solutions at $Ha = 3.406$ (24 full triangles) and $Ha = 3.403$ (48 open circles) beyond the 3rd and 4th bifurcations. At $Ha = 3.35$ and $Ha = 3.3$ chaotic flows are compared with the last regular solution of the Feigenbaum cascade in Fig. 10(c).

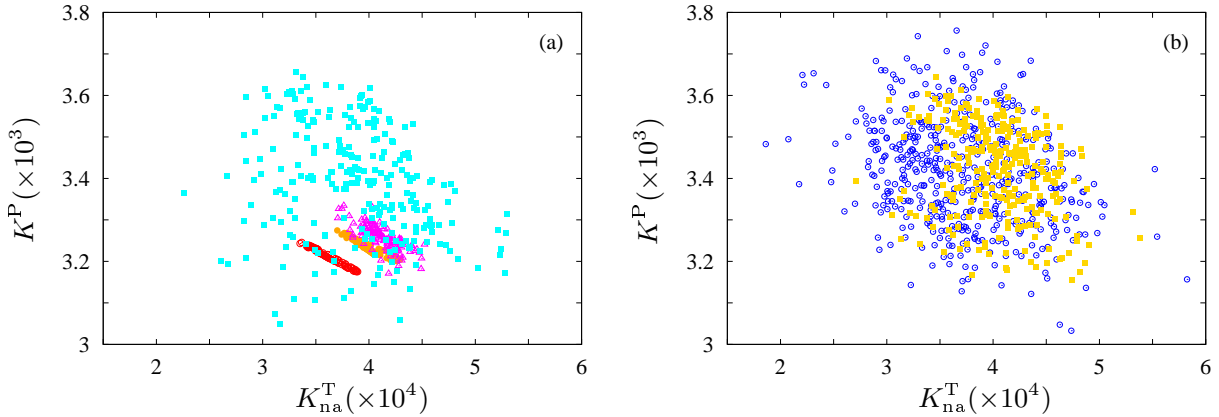


FIG. 11. Chaotic flows with $m = 2$ and with $m_{\max} = 2$, $m = 1$. The Poincaré sections are as in Fig. 4. (a) Chaotic flows with $m = 2$ at $Ha = 3.3$ (open circles), $Ha = 3$ (full circles), $Ha = 2.5$ (open triangles) and at $Ha = 1$ (full squares). (b) Comparison of chaotic purely hydrodynamic flows ($Ha = 0$) with $m = 2$ (open circles) and with $m_{\max} = 2$, $m = 1$ (full squares).

Finally, Fig. 11 investigates the Ha dependence of the Poincaré sections for chaotic flows down to $Ha = 0$. Volume averaged properties are considered as in Fig. 10. Figure 11(a) compares chaotic flows with $m = 2$ arising from the period doubling cascade to those with $m = 2$ more developed at lower Ha . By decreasing the magnetic field strength the chaotic flows become more oscillatory (and thus the cloud of points spreads over larger areas). The agreement between the Poincaré sections of flows belonging to Branch 5 (with $m = 2$) and those belonging to Branch 4 (with $m = 1$, $m_{\max} = 2$) is quite noticeable as seen on Fig. 11(b) displaying the Poincaré sections at $Ha = 0$. In agreement with Fig. 7(a) the chaotic flow with $m = 2$ becomes slightly more oscillatory than the corresponding flow with $m = 1$. For chaotic solutions on Branch 5 the number of spherical harmonics amplitudes is halved (as the azimuthal symmetry is $m = 2$) with respect to those on Branch 4 (with azimuthal symmetry $m = 1$). As flows on Branch 4 and Branch 5 have comparable energy (shown

on Fig. 2), this energy is shared out by more modes m in the case of Branch 4, which may facilitate the damping of the oscillations. The kinetic energy contribution of the $m = 2$ mode is comparable for both branches and the contribution of each of the remaining modes ($m = 1, 3, 4, 5, 6, 8$ for Branch 4 and $m = 4, 6, 8$ for Branch 5) is similar and roughly one order of magnitude smaller.

The flows with $m = 2$ considered in this section are all unstable. This has been checked by adding an $m = 1$ random perturbation which always grows, even with very small amplitude ($O(10^{-12})$). Perturbing the chaotic flows for $\text{Ha} \in [0, 1]$ with $m = 2$ gives rise to the chaotic flows with $m = 1$ lying on Branch 4. Because chaotic flows with $m = 2$ and with $m = 1$ have very similar kinetic energies and frequencies (see Fig. 8(b)) they are clearly related and thus Branch 4 seems to be related with Branch 5, that is, the unstable branch with $m = 2$.

E. Flow patterns

In this section the flow patterns for a chaotic solution are briefly described. The flow patterns do not change substantially for $\text{Ha} \in [0, 12.2]$. A comprehensive description of the topology of quasiperiodic waves, around $\text{Ha} \sim 5$, was performed in Ref. 42 so only few details are provided in this section. The studied range corresponds to the radial jet instability²⁴, which is nonaxisymmetric and asymmetric with respect the equatorial plane. A chaotic solution at $\text{Ha} = 0$ with $m = 1$ and $m_{\text{max}} = 2$ is considered. The contour plots of the nonaxisymmetric and total components of the radial velocity are displayed in the first and second rows of Fig 12. The third and fourth rows are analogous but for the kinetic energy. Three different sections -spherical, colatitudinal, and meridional- are selected on each row passing through a maximum of the corresponding field so the global picture emerges.

Quite regular nonaxisymmetric patterns are observed (1st/3rd rows) although the solution is chaotic. They compare very well with the patterns of quasiperiodic solutions studied in Ref. 42 (see for instance their Fig. 6). The flow consist of two main cells, as $m_{\text{max}} = 2$, but it is not invariant under π azimuthal rotations as it retains the $m = 1$ azimuthal symmetry (best shown on 3rd row). As it is usual for the spherical Couette system, with moderate $\text{Re} = 10^3$, the main flow is nearly axisymmetric consisting of a strong jet that is located close to equatorial latitudes (see meridional sections on 2nd/4th rows of Fig 12) and extends radially outwards from the inner sphere.

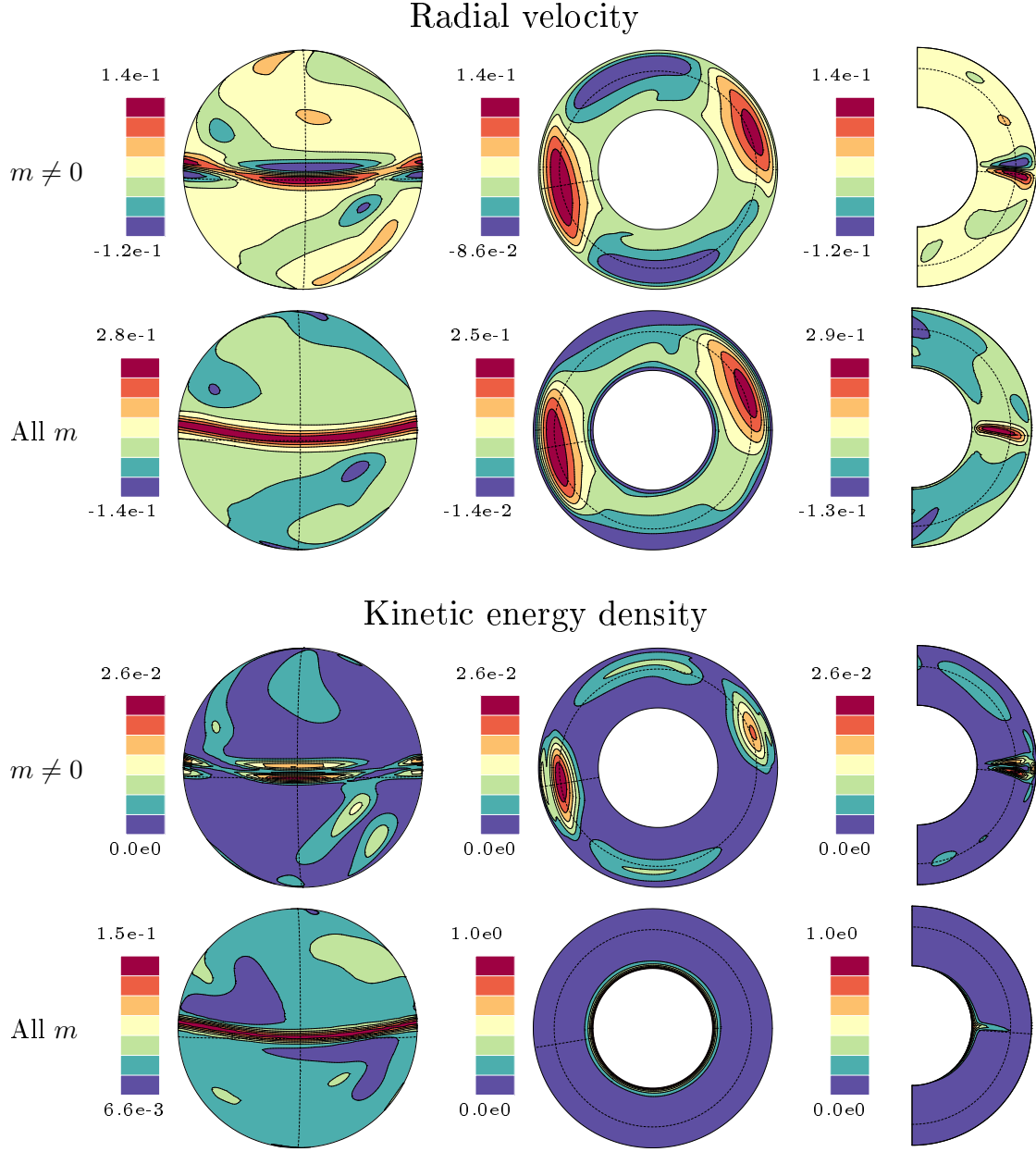


FIG. 12. Contour plots for a chaotic flow with $m = 1$, $m_{\max} = 2$ at $\text{Ha} = 0$. 1st/2nd rows: nonaxisymmetric and total components of the radial velocity. 3rd/4th rows: nonaxisymmetric and total components of the kinetic energy. Spherical, colatitudinal, and meridional sections are displayed on each row. For the nonaxisymmetric component every section is located in a such way that it is cutting a relative maxima of the respective field. The sections for the total component are located at the same positions than those of the nonaxisymmetric component to facilitate the comparison between both components. The position of the sections is marked with a dashed line.

V. DISCUSSION AND CONCLUSIONS

The present study constitutes a sequel of two previous papers (Refs. 18 and 42) where the dependence on the Hartmann number of rotating waves (periodic orbits) and modulated waves (invariant tori), respectively, were investigated in detail for the azimuthal symmetries $m = 2, 3, 4$ and for fixed $\text{Re} = 10^3$ and aspect ratio $\chi = 0.5$. In this new work we infer the existence of flows with complex temporal dependence arising from the branches of regular solutions previously computed in Refs. 18, 42 in the range $\text{Ha} \in [0, 6]$.

By means of direct numerical simulations we have been able to obtain several branches of modulated waves. Commonly, these solutions are invariant tori having two fundamental frequencies as in Ref. 42 or 49 (in the context of rotating thermal convection) but we have found modulated waves having 3 independent frequencies. According to Ref. 43, any small smooth perturbation applied to these 3-frequency solutions should provide a strange chaotic attractor, but it is not clear if this will happen in non-ideal physical systems⁴⁴. We have found, in agreement with Ref. 44, that three frequency solutions (3T) are typical in the magnetised spherical Couette system.

We have classified the flows by analysing the azimuthal symmetry m and the most energetic azimuthal wave number m_{max} . Three different classes of flows, with $m_{\text{max}} = 3$, with $m = 1, m_{\text{max}} = 2$ and with $m = 2$, are found and the bifurcations occurring on each of these classes are analysed. A rich variety of bifurcations and types of solutions have been found, including hysteretic behaviour. Secondary as well as tertiary Hopf bifurcations, period doublings, period doubling cascade and frequency locking are the typical mechanisms found to change the dynamics. Thanks to this rich dynamics several regions of multistability, comprising two, three and even four different types of solutions exist.

The appearance of multiple states in experimental flows strongly depends on the conditions assumed for the initial state⁶⁰, and in DNS the type of perturbation applied determines the type of mode that will be selected among the bifurcated solutions. Ultimately, the geometry of the stable invariant manifolds and their folding in the phase space determines the basin of attraction of each regular solution. In this way, the computation of these manifolds could help to understand why a given initial condition leads to the $m = 1, m_{\text{max}} = 2$ or to the $m = 1, m_{\text{max}} = 3$ branch, respectively.

Table III provides a quantitative overview of the different types of solutions found.

For $Re = 10^3$ and $\chi = 0.5$ the nonaxisymmetric radial jet instability extends through $Ha \in [0, 12.2]$ where 12.2 is the critical Hartmann number. This was found thanks to the linear stability analysis of the basic flow of Ref. 17. Then, the ratio of the interval of stability of a given type of flow to the total interval ($[0, 12.2]$ of the definition of the radial jet instability) provides a measure of the probability to obtain the given flow from a randomly distributed initial $Ha \in [0, 12.2]$. As it is shown in Table III a rather large probability of $1/5$ is expected for the case of three frequency solutions. This means that 3 frequency solutions are quite common in the spherical Couette system.

The comprehensive analysis presented here is of fundamental importance for current and future comparisons with the HEDGEHOG experiment, which is designed to run in a quasi-laminar regime ($Re \in [10^3, 10^4]$ and $Ha < 10^3$). The present study has considered a single $Re = 10^3$ as our focus was to study the dependence on the magnetic field strength. The analysis of the sensitivity to Re requires further research, especially for $Re \sim 10^4$. Previous numerical simulations (e.g., Ref. 15) have shown that the effect of increasing Re is to favour the appearance of flows with $m_{\max} = 2$ and, eventually, to develop turbulent motions. According to our results, modulated waves at $Ha < 5$ could be obtained in the experimental setup as they are the only stable and thus physically realisable flows. The frequency analysis we have performed has demonstrated that the frequency associated with the azimuthal drift of the flow is quite robust and remains nearly constant for $Ha \in [0, 6]$ and for each class of flows. For each complex wave this frequency is quite similar to that of the unstable rotating wave with $m = m_{\max}$ at the same Ha .

Moreover, the frequency analysis provides the time scales of the modulation thus constraining the required duration of the related experimental runs. For instance, in the case of flows with $m = 1$, $m_{\max} = 2$ the main frequency of modulation for 2T solutions at $Ha < 6$ is smaller than 2 mHz, which requires time scales larger than 10 min. Then, the experiment should run during almost a day to capture at least 100 modulation periods. Very long experimental runs should be avoided because of the signal quality of the ultrasonic Doppler velocimetry (UDV) measurements degrades over time (see Ref. 16 for details). The latter is caused by the evolution of tracer particles (oxydes, solid binary phase combinations of GaInSn) distribution within the liquid metal. The tracer particles sediment during the experimental run so that the signal quality decreases. We notice that relative variations of Re and Ha due to variations of the viscosity (0.5%), conductivity (0.1%) or density (0.01%)

TABLE III. Occurrence of the different types of temporal dependence. The interval of definition of the nonaxisymmetric radial jet instability is $\text{Ha} \in [0, \text{Ha}_c)$ with $\text{Ha}_c = 12.2$ being the critical Hartmann number¹⁷. The percents represent the ratio between the length of the interval of stability of a given type of flow with respect the whole interval of definition of the radial jet instability.

Flow class	rotating wave	modulated wave 2T	modulated wave 3T	Chaos
$m_{\max} = 3$	67.6%	41.5%	17.3%	
$m = 1, m_{\max} = 2$		49.1%	4.4%	8.2%

related with temperature changes (around 5 degrees in the laboratory during a day) lead to a total variation of the dimensionless parameters of about $\mathcal{O}(1\%)$. This is an acceptable inconvenience as we assume a sufficiently smooth transition for the bifurcation diagrams in the parameter space (see for instance Fig. 2), except close to bifurcation points.

ACKNOWLEDGMENTS

F. Garcia kindly acknowledges the Alexander von Humboldt Foundation for its financial support. This project has also received funding from the European Research Council (ERC) under the European Unions Horizon 2020 research and innovation programme (grant agreement No 787544).

REFERENCES

- ¹K. Stewartson, *J. Fluid Mech.* **26**, 131 (1966).
- ²E. Dormy and A. M. Soward, eds., *Mathematical Aspects of Natural Dynamos*, The Fluid Mechanics of Astrophysics and Geophysics, Vol. 13 (Chapman & Hall/CRC, Boca Raton, FL, 2007).
- ³C. A. Jones, *Ann. Rev. Astron. Astrophys.* **43**, 583 (2011).
- ⁴G. Rüdiger, *Differential Rotation and Stellar Convection: Sun and Solar-type Stars*, Fluid mechanics of astrophysics and geophysics (Gordon and Breach Science Publishers, 1989).
- ⁵A. Gailitis, O. Lielausis, E. Platācis, G. Gerbeth, and F. Stefani, *Rev. Mod. Phys.* **74**, 973 (2002).

- ⁶A. Brandenburg and K. Subramanian, Phys. rep. **417** (2005).
- ⁷K. Moffat and E. Dormy, *Self-Exciting Fluid Dynamos*, Cambridge Texts in Applied Mathematics (Cambridge University press, 2019).
- ⁸S. A. Balbus and J. F. Hawley, Astrophys. J. **376**, 214 (1991).
- ⁹H. Ji and S. Balbus, Phys. Today **66**, 27 (2013).
- ¹⁰F. Stefani, T. Gundrum, G. Gerbeth, G. Rüdiger, M. Schultz, J. Szklarski, and R. Hollerbach, Phys. Rev. Lett. **97**, 184502 (2006).
- ¹¹F. Stefani, G. Gerbeth, T. Gundrum, R. Hollerbach, J. Priede, G. Rüdiger, and J. Szklarski, Phys. Rev. E **80**, 066303 (2009).
- ¹²M. Seilmayer, V. Galindo, G. Gerbeth, T. Gundrum, F. Stefani, M. Gellert, G. Rüdiger, M. Schultz, and R. Hollerbach, Phys. Rev. Lett. **113**, 024505 (2014).
- ¹³D. R. Sisan, N. Mujica, W. A. Tillotson, Y. M. Huang, W. Dorland, A. B. Hassam, T. M. Antonsen, and D. P. Lathrop, Phys. Rev. Lett. **93**, 114502 (2004).
- ¹⁴R. Hollerbach, Proc. Roy. Soc. Lond. A **465**, 2003 (2009).
- ¹⁵C. Gissinger, H. Ji, and J. Goodman, Phys. Rev. E **84**, 026308 (2011).
- ¹⁶C. Kasprzyk, E. Kaplan, M. Seilmayer, and F. Stefani, Magnetohydrodynamics **53**, 393 (2017).
- ¹⁷V. Travnikov, K. Eckert, and S. Odenbach, Acta Mech. **219**, 255 (2011).
- ¹⁸F. Garcia and F. Stefani, Proc. Roy. Soc. Lond. A **474**, 20180281 (2018).
- ¹⁹G. Schrauf, J. Fluid Mech. **166**, 287 (1986).
- ²⁰O. Y. Zikanov, J. Fluid Mech. **310**, 293 (1996).
- ²¹R.-J. Yang and W.-J. Luo, Theoret. Comput. Fluid Dynamics **16**, 115 (2002).
- ²²L. Yuan, Phys. Fluids **24**, 124104 (2012).
- ²³P. Wulf, C. Egbers, and H. J. Rath, Phys. Fluids **11**, 1359 (1999).
- ²⁴R. Hollerbach, M. Junk, and C. Egbers, Fluid Dyn. Res. **38**, 257 (2006).
- ²⁵S. Abbas, L. Yuan, and A. Shah, Fluid Dyn. Res. **50**, 025507 (2018).
- ²⁶A. Barik, S. A. Triana, M. Hoff, and J. Wicht, J. Fluid Mech. **843**, 211 (2018).
- ²⁷J.-P. Eckmann, Rev. Modern Phys. **53**, 643 (1981).
- ²⁸J. Wicht, J. Fluid Mech. **738**, 184 (2014).
- ²⁹R. Hollerbach and S. Skinner, Proc. Roy. Soc. Lond. A **457**, 785 (2001).
- ³⁰X. Wei and R. Hollerbach, Acta Mech. **215**, 1 (2010).
- ³¹A. Figueroa, N. Schaeffer, H.-C. Nataf, and D. Schmitt, J. Fluid Mech. **716**, 445 (2013).

- ³²E. J. Kaplan, Phys. Rev. E **85**, 1 (2014).
- ³³E. J. Kaplan, H.-C. Nataf, and N. Schaeffer, Phys. Rev. Fluids **3**, 034608 (2018).
- ³⁴D. Brito, T. Alboussière, P. Cardin, N. Gagnière, D. Jault, P. La Rizza, J.-P. Masson, H.-C. Nataf, and D. Schmitt, Phys. Rev. E **83**, 066310 (2011).
- ³⁵D. G. Meduri, F. Lignières, and L. Jouve, Phys. Rev. E **100**, 013110 (2019).
- ³⁶D. Rand, Arch. Ration. Mech. An. **79**, 1 (1982).
- ³⁷J. D. Crawford and E. Knobloch, Ann. Rev. Fluid Mech. **23**, 341 (1991).
- ³⁸R. E. Ecke, F. Zhong, and E. Knobloch, Europhys. Lett. **19**, 177 (1992).
- ³⁹M. Golubitsky, V. G. LeBlanc, and I. Melbourne, J. Nonlinear Sci. **10**, 69 (2000).
- ⁴⁰M. Golubitsky and I. Stewart, *The symmetry perspective: From equilibrium to chaos in phase space and physical space*. (Birkhäuser, Basel, 2003).
- ⁴¹D. Schmitt, T. Alboussière, D. Brito, P. Cardin, N. Gagnière, D. Jault, and H.-C. Nataf, J. Fluid Mech. **604**, 175 (2008).
- ⁴²F. Garcia, M. Seilmayer, A. Giesecke, and F. Stefani, J. Nonlinear Sci. **29**, 2735 (2019).
- ⁴³S. Newhouse, D. Ruelle, and F. Takens, Commun. Math. Phys. **64**, 35 (1978).
- ⁴⁴C. Grebogi, E. Ott, and J. A. Yorke, Phys. Rev. Lett. **51**, 339 (1983).
- ⁴⁵J. M. Lopez and F. Marques, Phys. Rev. Lett. **85**, 972 (2000).
- ⁴⁶O. Batiste, E. Knobloch, I. Mercader, and M. Net, Phys. Rev. E **65**, 0163031 (2001).
- ⁴⁷A. Randriamampianina, W.-G. Früh, P. L. Read, and P. Maubert, J. Fluid Mech. **561**, 359 (2006).
- ⁴⁸L. Oteski, Y. Duguet, L. Pastur, and P. Le Quéré, Phys. Rev. E **92**, 043020 (2015).
- ⁴⁹F. Garcia, M. Net, and J. Sánchez, Phys. Rev. E **93**, 013119 (2016).
- ⁵⁰J. Laskar, Celestial Mech. Dyn. Astr. **56**, 191 (1993).
- ⁵¹N. B. Morley, J. Burris, L. C. Cadwallader, and M. D. Nornberg, Review of Scientific Instruments **79**, 056107 (2008).
- ⁵²M. Frigo and S. G. Johnson, Proceedings of the IEEE **93**, 216 (2005), special issue on "Program Generation, Optimization, and Platform Adaptation".
- ⁵³K. Goto and R. A. van de Geijn, ACM Trans. Math. Softw. **34**, 1 (2008).
- ⁵⁴F. Garcia, M. Net, B. García-Archilla, and J. Sánchez, J. Comput. Phys. **229**, 7997 (2010).
- ⁵⁵Y. Saad and M. H. Schultz, SIAM J. Sci. Stat. Comput. **7**, 865 (1986).
- ⁵⁶Y. Plevachuk, V. Sklyarchuk, S. Eckert, G. Gerbeth, and R. Novakovic, J. Chem. Eng. Data **59**, 757 (2014).

- ⁵⁷G. Gómez, J. M. Mondelo, and C. Simó, *Discrete Cont. Dyn. B* **14**, 41 (2010).
- ⁵⁸J. Sánchez, M. Net, B. García-Archilla, and C. Simó, *J. Comput. Phys.* **201**, 13 (2004).
- ⁵⁹F. Garcia, J. Sánchez, E. Dormy, and M. Net, *SIAM J. Appl. Dynam. Systems* **14**, 1787 (2015).
- ⁶⁰K. Nakabayashi and Y. Tsuchida, *J. Fluid Mech.* **295**, 43 (1995).